ELSEVIER

CrossMark

Trends and perspectives in solid-state wetting / Mouillage solide–solide : tendances et perspectives

Dynamics and instability of solid-state dewetting

Démouillage à l'état solide : dynamique et instabilités

Fabien Cheynis, Frédéric Leroy, Pierre Müller *

Aix–Marseille University, CINaM UMR CNRS 7325, case 913, campus de Luminy, 13288 Marseille cedex, France

A B S T R A C T

Spontaneous dewetting of solid thin films proceeds by edge retraction of film edges and/or by heterogeneous void growth. Classical 1D and 2D continuous models of the evolution of a dewetting film, based on surface diffusion mechanisms, predict that in the long-time limit dewetting obeys universal scaling laws. In this paper, we review 1D and 2D predictions and recent experimental results. For this purpose, using $Si(001)/SiO_2$ and $Ge(001)/SiO_2$ single-crystalline thin films in different geometries, we have been able to compare theoretical predictions to experimental results obtained by combining in situ LEEM and ex situ AFM measurements. For dewetting from film edges, experimental results partially differ from continuous models predictions. More precisely, because of the crystallographic anisotropy: (i) the facetted edges remain stable during dewetting (they simply recede at constant shape) while poorly or un-facetted edges are unstable (they recede by finger formation); (ii) rim formation, induced by mass-conservation condition, proceeds in a layer-by-layer mode and is limited by 2D nucleation properties on the top of the rim; (iii) the island generation mechanism differs from the mass shedding behaviour predicted by 1D models. For dewetting mechanisms involving void growth, different behaviours are reported and discussed. For thin $Si(001)/SiO_2$ films, the corners of the opening square-shaped voids lead to a local destabilisation of the growing voids. For thin $Ge(001)/SiO_2$ films, the side of the voids invariably turns instable and forms tip dendrites whose branch density depends on the temperature and the initial film thickness. Finally, ultra-thin films, more sensitive to local fluctuations, dewet in a fractal geometry.

© 2013 Académie des sciences. Published by Elsevier Masson SAS. All rights reserved.

R É S U M É

Le démouillage spontané de films minces solides s'effectue par retractation des bords du film et/ou par croissance hétérogènes de lacunes. Les modèles classiques continus décrivant le démouillage sont basés sur la diffusion de surface et prédisent des lois de comportement universelles. Nous décrivons quelques unes de ces prédictions et les comparons à de récents résultats expérimentaux obtenus sur des films monocristallins de $Si(001)/SiO_2$ et de $Ge(001)/SiO_2$ étudiés par micoscopie à électrons lents (LEEM) *in-situ* et par microscopie à force atomique (AFM) *ex-situ*. Les résultats expérimentaux ainsi obtenus diffèrent des prédictions théoriques. Plus précisément, à cause de l'anisotropie cristalline : (i) les fronts de démouillage facetés restent stables pendant le démouillage et reculent à forme constante alors que les fronts de démouillage non facetés sont instables et reculent en formant des digitations, (ii) le bourrelet qui, pour des raisons de conservation de la masse, se forme pendant le démouillage s'épaissit via un mode de croissance couche

* Corresponding author.
E-mail address: muller@cinam.univ-mrs.fr (P. Müller).

par couche limité par la nucléation bidimensionnelle sur la face sommitale du bourrelet, (iii) le mécanisme final de génération d'ilots tridimensionnels diffère de celui prédit par les modèles continus. Nous dicutons également les mécanismes de démouillage procédant par ouverture de lacunes. Dans le cas de Si(001)/SiO₂, les lacunes de démouillage, initialement carrées, sont localement déstabilisées par les coins alors que dans le cas de Ge(001)/SiO₂, les bords des lacunes deviennent invariablement instables conduisant à la formation de dendrites dont la densité dépend de la température et de l'épaisseur du film. Finalement, nous discutons quelques cas de films ultraminces, plus sensibles à des variations locales d'épaisseur, et formant par démouillage des structures fractales ou labyrinthiques.

1. Introduction

The energetic criterion to obtain a 2D film in a layer-by-layer growth mode can be written, close to equilibrium conditions, as $E_s = \gamma_A + \gamma_{AB} - \gamma_B < 0$, where γ_A is the surface free energy density of the deposited film A, γ_B the surface energy density of the substrate B, and γ_{AB} is the interfacial energy [1]. E_s is called the wetting factor. Clearly, the criterion $E_s < 0$ cannot be satisfied for all couples (A, B). Thus, in numerous thin film systems, the flat 2D film is a non-equilibrium configuration. The process by which a metastable film agglomerates into an assembly of 3D nanocrystals to reach a more stable configuration is called dewetting.

While the dewetting of liquid layers is now well understood (for a review see [2]), for a few years there has been a new craze for studying the dewetting of solid thin films [3–10], since they are crucial elements in numerous technologies.

Spontaneous dewetting is generally initiated by heterogeneous nucleation of voids at randomly distributed defects followed by void opening. Dewetting may also start at specific defects such as film edges.

Since dewetting generally occurs at defects, it may be influenced by substrate step structure [11], substrate morphology [12,13], elastic properties [14–16], grain boundaries in the film [17], or even the film's geometry via its edges [18]. A careful experimental study of dewetting dynamics thus requires to select perfectly characterised materials in order to discriminate against these various possible effects. The experimental investigations we report here have been carried out on Si(001)/SiO₂ and Ge(001)/SiO₂ thin films. More precisely, we have selected Silicon-On-Insulator (SOI) and Germanium-On-Insulator (GeOI or GOI) thin films fabricated by means of the Smartcut process at CEA–LETI (Grenoble, France) by molecular bonding. These samples are constituted of a Si(001) or a Ge(001) single-crystalline film [19] (in order to avoid grain boundary effects) bonded onto a $\gtrsim$150-nm-thick amorphous silicon dioxyde layer (in order to avoid interfacial structure effects) supported by a Si substrate. Furthermore, no residual stress in the film has been evidenced.

In this paper, we will consider two dewetting mechanisms: (i) dewetting by film edge retraction from a 1D well-oriented trench (Section 3) and (ii) spontaneous dewetting by heterogeneous void opening (Section 4). In each case, we will recall classical theoretical formulations that allow one to catch the essential of the underlying physics, then we will report experimental results recorded on semiconductors films. Moreover, in the conclusion, we will also discuss other mechanisms for which grain boundaries and substrate structure play a role.

2. Experiments

For Si films, a standard ex situ chemical cleaning procedure leads to the formation of an oxidised capping layer. The so-prepared samples are introduced in an ultra-high vacuum chamber having a base pressure in the low 10^{-10} Torr range, then degassed at 500–600 °C during several hours. The silicon oxide is then simply removed by annealing the film at 700 °C during, typically, 20 min. The thickness of the Si film is about 22 ± 2 nm. For Ge films, the in situ treatment consists in an ion bombardment ($P_{Ar^+} \simeq 4.10^{-7}$ Torr, 1 keV, $I_e \simeq 10$–13 µA) followed by annealing at 400 °C during 30 min. The thickness of the so-obtained Ge film is about 20 nm.

Most of the experimental results we report in this paper have been obtained by combining in situ Low-Energy Electron Microscopy (LEEM) observations and ex situ Atomic Force Microscopy (AFM) observations. LEEM experiments allow direct measurement of the kinetics [9,20–23], contrary to previous works in which the kinetics is indirectly measured. For instance, in Ref. [12], the kinetics is obtained from the evolution of the electrical resistance versus time and, in Ref. [24], it is measured by the evolution of the optical reflectivity of the surface.

3. Dewetting dynamics of film edges

Recent experimental observations on Si(001)/SiO₂ films with artificial trenches oriented along ⟨100⟩ and ⟨110⟩ directions edges in the Si film fabricated by e-beam lithography [25] suggest that the stability condition of a crystallised dewetting front is governed by the presence of crystallographic atomically flat facets having the front direction as a common zone axis. Fronts along facetted orientations simply recede, keeping the same orientation during dewetting, while other front orientations develop morphological instabilities. More specifically, ⟨110⟩-oriented dewetting fronts are the common zone axis of {111} and {113} facets, and thus are stable, while the ⟨100⟩-oriented fronts break down during dewetting, as shown
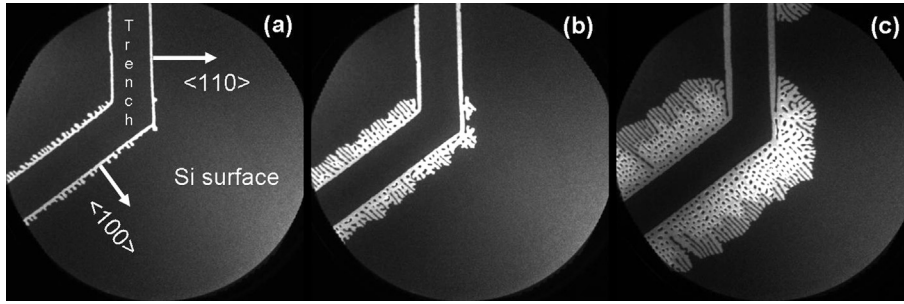
Fig. 1. Dewetting from artificial edges etched by lithography in the Si(001)/SiO$_2$ film (field of view: 50 μm). The trench exhibits artificial ⟨110⟩ and ⟨100⟩ edges. The ⟨110⟩ edge is stable and simply recedes, keeping a straight front while the ⟨100⟩ front is destabilised. Note that a local destabilisation of the ⟨110⟩ front may emerge from a local defect. Dewetting duration: (a) $t \approx 5$ min, (b) $t \approx 25$ min, (c) $t \approx 60$ min.

in Fig. 1. The LEEM sequence (in which Si corresponds to dark zones while the decovered SiO$_2$ substrate is bright) shows that dewetting initiates at the artificial fronts. It can be easily seen that, while the ⟨110⟩-oriented front recedes at constant shape and slow velocity, the ⟨100⟩-oriented front dewets with a greater velocity, but does not remain straight. More precisely, during dewetting, the ⟨100⟩ front forms elongated Si structures (called Si fingers) that periodically break down into nano-islands of Si (black dots in Fig. 1). In the following, we will separately consider both cases of stable ⟨110⟩-oriented fronts (Section 3.1) and unstable ⟨100⟩-oriented fronts (Section 3.2). Each subsection will start with a short review of numerical results.

3.1. Kinetics of dewetting of a stable front

3.1.1. 1D continuous model

Contrary to liquids where dewetting kinetics is dominated by hydrodynamics [26], dewetting of solid films is usually a capillary-driven surface diffusion mechanism [22]. It means that, for an isotropic solid film, the profile evolution of the dewetting film obeys the classical Mullins equation [27]:

$$V_n = -B\nabla_s^2 \kappa \tag{1}$$

where V_n is the velocity of the surface normal, $\nabla_s^2 \kappa$ the surface Laplacian of the curvature κ at the surface, $B = D_s \gamma_A \Omega^2 n / k_B T$ a kinetics coefficient where D_s is the surface diffusion constant, n the number of atoms per unit area, γ_A the surface energy density of the film A and Ω an atomic volume. Even if many papers [28–32] have been devoted to the resolution of this equation, we discuss its main predictions in a simplified approach.

In a 1D case, the local height of the film above the substrate reads $h(x, t)$, where x and t, respectively, are spatial and temporal variables. In the small slope limit ($\partial h / \partial x < 1$), Eq. (1), written in the moving frame associated with the triple line $x_0(t)$, reduces to:

$$\frac{dh}{d\tau} = -\frac{\partial^4 h}{\partial x^4} + \frac{dx_0}{d\tau}\frac{\partial h}{\partial x} \tag{2}$$

where now the time τ is expressed in units of h_0^4/B and the spatial length in units of h_0 (the initial thickness of the film). Now $x = 0$ defines the position of the triple line.

This equation can be solved with the following geometrical boundaries conditions $h(0, \tau) = 0$ and $h(x \to \infty) = h_0$ completed by two others. The first one $\frac{\partial h}{\partial x}|_{x=0} = \tan\theta$ defines the Young equilibrium wetting angle. The contact angle equilibrates quasi-instantaneously as compared to the general profile evolution so that, except for transitory states, the Young angle given by $\cos\theta = \frac{\gamma_B - \gamma_{AB}}{\gamma_A}$ can be fixed [29,32]. The last boundary condition comes from the absence of a source of matter at the triple line [28]. It reads $\frac{\partial \mu}{\partial x} = 0$, where μ is the curvature-dependent local chemical potential. This becomes in the small slope approximation $\frac{\partial^3 h}{\partial x^3}|_{x=0} = 0$. The diffusion equation (Eq. (2)) combined with these boundaries conditions allows us to write the velocity of the triple line as:

$$V_t = \frac{dx_0}{d\tau} = \frac{1}{\tan\theta}\frac{\partial^4 h}{\partial x^4}\bigg|_{x=0}$$

The numerical results are reported as a sequence of profiles in Fig. 2. It can be seen that solid-state dewetting is controlled by the kinetics of a receding rim: the film material removed from the substrate during the dewetting accumulates into a thickening rim. The receding rim is preceded by a valley. When the valley reaches the substrate, the film is broken and generates a crystalline nanowire parallel to the film front. The new film edge is thus quickly equilibrated to reach its equilibrium Young angle, and then the process is repeated from the new film front. This periodic island formation by mass shedding is numerically described by [30,32].
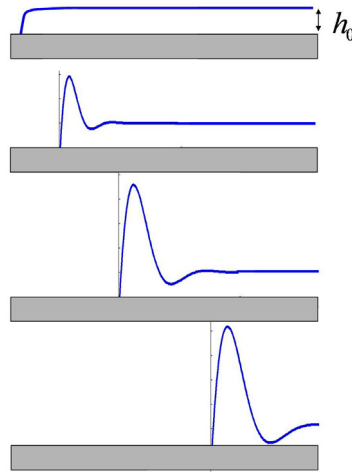
Fig. 2. Sketch of the profile evolution versus time. Note the formation of a thickening rim followed by a depression at the origin of film breaking.
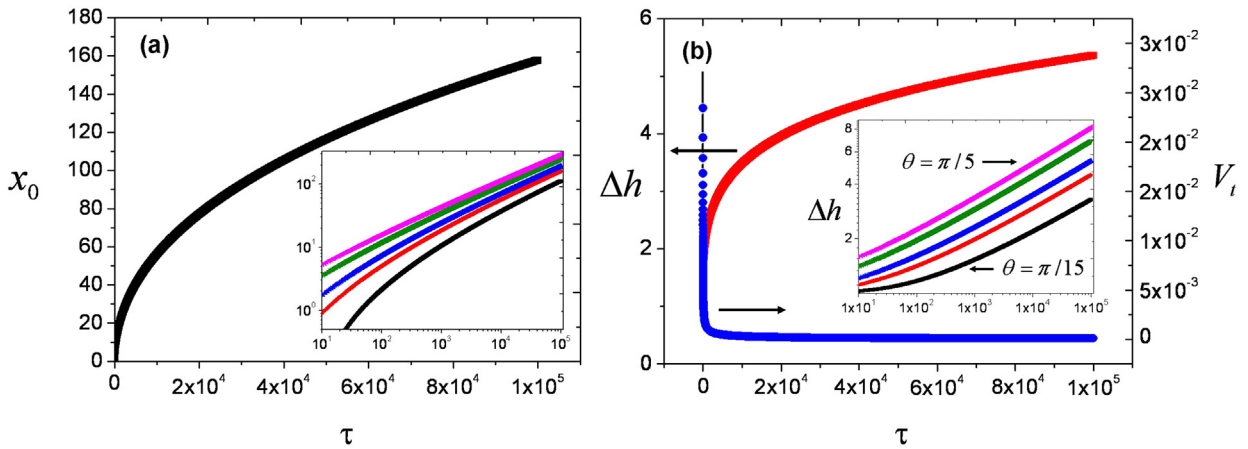

Fig. 3. Numerical results of the integration of Eq. (2): (a) $x_0(\tau)$, (b) $\Delta h(\tau) = h_{max} - h_0$ (rim height) and V_t. Calculations are performed for a Young angle $\theta = \pi/8$. In the inset are reported in a log–log diagram $x_0(\tau)$ and $\Delta h(\tau)$ calculated for $\theta = \pi/15$ (bottom curves), $\pi/8$, $\pi/6$ and $\pi/5$ (top curves). $x_0(\tau)$ and $\Delta h(\tau)$ increase with θ. Color available online.

In Fig. 3(a,b), we plot the time evolution of the triple line $x_0(\tau)$, the rim thickening $h(\tau)$ and the velocity of the triple line $V_t(\tau)$ for a given Young angle. As a general rule of thumb, the thicker the rim, the smaller the velocity of the triple line. This illustrates the fact that the velocity of the triple line is controlled by the rim thickening mechanism. In the inset of Fig. 3, we plot $x_0(\tau)$ and $h(\tau)$ in a log–log diagram for Young angles varying from $\pi/15$ to $\pi/5$. These results show that in the long-time limit, dewetting obeys universal scaling laws: (i) the height of the rim thickens as $\tau^{\sim 0.23}$, (ii) the triple line position recedes as $\tau^{\sim 0.43}$, and (iii) the local valley (not shown) deepens as $t^{\sim 0.26}$. Note that the scaling law $x_0(\tau) \propto t^{2/5}$ has already been reported by [30], but can also be predicted by using simpler geometrical models in which the local geometry of the rim is fixed [33,3].

Obviously, for facetted materials, the Mullins equation cannot be valid, since the standard concept of curvature-driven surface diffusion cannot be directly applied to an anisotropic material. Dornel et al. [32] have developed a specific method to calculate numerically a surface chemical potential change that is valid for anisotropic materials. They found the same time exponents 0.23 and 0.43 for the height of the receding rim and for the triple line position, respectively. The scaling law $x_0 \propto t^{0.44}$ has been found by [34] using a specific model of retraction of a fully facetted edge. Note that inclusion of non-linear effects does not drastically change these main behaviours [30,35].

3.1.2. Experimental results

As we show in Fig. 1, $\langle 110 \rangle$-oriented film edges of Si(001)/SiO$_2$ film dewet by a retraction of the moving front with the formation of a thickening rim. It is thus meaningful to compare experimental results obtained for such stable fronts to the prediction of the 1D model developed in the previous section.

For this purpose, we report in Fig. 4 $x_0(t)$ and $h(t)$ evolutions measured from LEEM movies (for experimental details, see Ref. [25]). The triple line's position behaves as $(190 \pm 20)t^{0.37 \pm 0.03}$, in fair agreement with the scaling law predicted by the
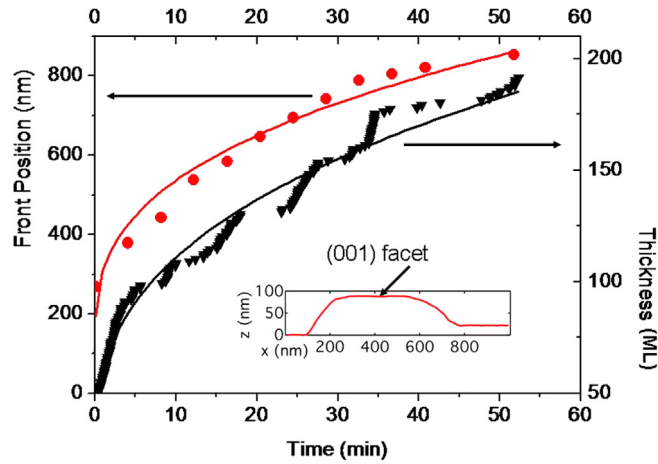
Fig. 4. Experimental results $x_0(t)$ and $\Delta h(t)$ for stable $\langle 110 \rangle$ fronts. Inset: film profile of the dewetting front recorded by AFM.

1D model $x_0(t) \propto t^{0.43}$. The rim thickens more rapidly in experiments ($h(t) \propto t^{0.38 \pm 0.02}$) than in the 1D model ($h(t) \propto t^{0.23}$). Two contributions may be at the origin of this discrepancy. First, as revealed by the AFM profile in the inset of Fig. 4, the rim is facetted with a top (001) facet. LEEM movies recorded in dark-field mode by selecting the half-integer diffraction spot associated with the (1×2) reconstruction of the Si(001) surface show that the top facet of the rim alternatively flashes from bright to dark [25]. This means that the rim thickens in a layer-by-layer growth mode with alternatively 1×2 then 2×1 surface reconstructions [25]. Such a facetted rim has also been reported for SOI [32] and for other systems, as for instance Ni/MgO [36] and Fe–Au on sapphire [37]. However, to the best of our knowledge, this layer-by-layer growth of the top facet of the rim has not been reported in the literature. Second, we have no clear experimental evidence of a systematic occurrence of a valley behind the rim. Obviously, this absence of depletion prevents the mass shedding mechanism at the origin of the nanowire formation described by [30]. These two effects contribute to accumulate more material on the top of the rim than expected in the continuous model. To be thorough, Dornel observed in some cases the occurrence of a deep valley and a mass shedding effect on the SOI system when annealed under H_2 partial pressure, but not for all receding rims [38]. The explanation brought forward was a probable carbon contamination related to surface energy changes. Finally, a careful comparison, in our LEEM data, between the time necessary to nucleate a 2D island on the top facet of the rim and the time necessary to complete a new top layer shows that the thickening kinetics is limited by the 2D nucleation on the top facet of the rim [25].

3.1.3. Discussion

Since the classical Mullins model depicted in Eq. (1) does not contain the layer-by-layer thickening mechanism encountered in experiments, Pierre-Louis et al. [39,40] have proposed a new model for the evolution of the rim height based on 2D nucleation theory and a diffusion-limited mechanism. More precisely, as in the experiments, the rim height increases via the nucleation of a new layer on the top facet of the rim. Using a 1D model in which the rim is modeled by a box-shaped crenel of width ℓ, the height variation is written as $\frac{\partial h}{\partial t} = (V_{zip} J)^{1/2}$, where V_{zip} is the zipping velocity of the growing monolayer on the top facet along the rim and J is the monolayer island nucleation rate per unit of length. The nucleation rate is calculated by using classical nucleation theory, within the capillary approximation. It reads $J = K(\frac{\Delta \mu}{k_B T})^{3/2} e^{-\Delta G / k_B T}$, where $\Delta \mu = E_s / h$ is the local chemical potential per unit volume at the edge of the rim, with $E_s = \gamma_{Si} + \gamma_{int} - \gamma_{ox}$ the wetting factor. The factor $K = \ell D_s c_{eq} \frac{k_B T}{\pi \beta^2}$ depends on the surface diffusion coefficient D_s, the adatom concentration c_{eq} and β the edge energy density of the 2D nuclei (assumed to be circular). ΔG is the nucleation work that has to be overpassed to obtain a nucleus that spontaneously grows. The zipping velocity is evaluated as $V_{zip} = D_s c_{eq} (\Delta \mu - \mu_{eq})$ where the local chemical potential μ is curvature dependent. The maximum velocity thus reads $V_{zip} = \frac{D_s c_{eq}}{4 a^2 \beta} (\frac{E_s}{h k_B T})^2$. Putting all together, Pierre-Louis et al. [39,40] obtain for multiple nucleation events:

$$\frac{\partial h}{\partial t} = \frac{D c_{eq}}{2 \pi^{1/2} \beta^{3/2} (k_B T)^{1/4}} \ell^{1/2} \left(\frac{E_s}{h} \right)^{7/4} e^{-\Delta G / 2 k_B T} \tag{3}$$

where $\Delta G = \pi \beta^2 h / k_B T E_s$ is the thickness-dependent nucleation work calculated for circular 2D nuclei. Note that the nucleation rate on the top facet decreases with the height of the rim, as experimentally reported, for instance, for an ice film on Pt(111) [41].

For Si(001) surface, the mean step energy is quite small ($\beta = 6$ meV/Å) [42] and $E_s \approx 14$ eV nm^{-2} [22], so that $\Delta G / 2 k_B T \to 0$. In this case, Eq. (3) can be analytically integrated, giving $h \propto t^\alpha$, with a universal exponent $\alpha = 4/11 = 0.36$ closer to the experimental result of 0.38 ± 0.02 than obtained from the continuous model. However, the calculated prefactor is ten orders of magnitude too high. This discrepancy is due to the small value of the step energy β, which, in the

Table 1
Asymptotic behaviours obtained from Eq. (4) combined to mass conservation.

Geometrical assumption	Rim position	Rim height
$\ell = C^{te}$	$x_0 \sim t^{1/3}$	$h \sim t^{1/3}$
$\ell/h = C^{te}$	$x_0 \sim t^{2/5}$	$h \sim t^{1/5}$
$h = C^{te}$	$x_0 \sim t^{1/2}$	–
$h = C^{te}$ and $\ell = C^{te}$	$x_0 \sim t$	–

framework of capillary theory, gives a critical radius of roughly one or two atoms, i.e. beyond the domain of validity of the capillary theory. It is thus necessary (at least for silicon) to substitute a chemical approach for the classical capillary theory. For this purpose, using Zinsmeister's [43] or Venable's [44] results, we can write the nucleation rate as $I = K^\circ F^{i+1}$, where F is the rate of arrival of adatoms, i the critical nucleus size (we will take unity), and K° a coefficient depending on the adatom surface diffusion constant, the capture number and the statistical weights. As a rough estimate, we will assume that $F = ZE_s/hk_BT$, where Z, estimated from the experimental time necessary to nucleate a new top layer, is a constant of the order of 1 nm^3 s^{-1}. We will consider that $V_{zip} = \frac{D_s c_{eq}}{k_B T}\kappa(\frac{E_s}{h})$ or in other words that the zipping velocity is simply proportional to the adatom diffusion rate (it should be exact for rough steps). Putting all together, we find $h \propto t^\alpha$, with $\alpha = 2/5 = 0.4$, in agreement with experimental results, with a prefactor that has a good order of magnitude, even if it cannot be exactly evaluated, due to poorly measured quantities such as capture numbers, statistical weights, etc.

Note that in Refs. [22,23,25], we have developed a 1D analytical model in which we assume, in a simple geometrical configuration of a box-shaped crenel rim, that the velocity of the triple line is equal to the thermodynamic force E_s/h times an effective surface-diffusion-based mobility calculated from the average time necessary for an adatom to cross over the top facet of the rim. We obtain:

$$\frac{dx_0}{dt} = D_s c_{eq} E_s \Omega^2 / \ell a^2 h^2 k_B T \tag{4}$$

This velocity expression can be analytically integrated in few asymptotic situations reported in Table 1.

Experimental data and asymptotic power laws reported in Table 1 are in fair agreement when the rim recedes at constant width since we find $x(t) \approx 190 t^{1/3}$ and $h(t) \approx 10 t^{1/3}$, while experiments give (see Fig. 4) $x(t) \approx 190 t^{0.37\pm0.03}$ and $h(t) \approx 6 t^{0.38\pm0.02}$, what is satisfactory for this simple model.

Let us, however, underline the main differences between the aforementioned models. In the simple 1D analytical model, it is assumed that the mobility of the front edge is simply limited by the diffusion across the width of the rim with a characteristic time $\tau = \ell^2/D_s$. The model developed by Pierre-Louis et al. considers the 2D nucleation events on the rim. The limiting step is thus the zipping time for a 2D monolayer to spread along the front edge, which depends obviously on the nucleation mode (multi-nucleation or single nucleus formation) on the top of the rim. This model should be better than the geometric one, but for Si/SiO$_2$, the capillary theory used to establish Eq. (3) is no more valid and a complete chemical approach has to be developed. Such approaches lead to Hertz–Knudsen-type laws, whose analytical shape is close to the expression coming from the simple geometric model.

3.2. Dewetting dynamics of an unstable front

As seen in Fig. 1, Si⟨100⟩-oriented fronts are unstable and dewet with a greater velocity than stable fronts. The fronts do not remain straight, but form elongated structures called Si fingers, into which the mass of the film is efficiently transferred (see Fig. 5a). Such an instability is associated with a rim-height instability [31]. Indeed, for a ⟨100⟩-oriented edge, the rim does not recede with a uniform height, but locally thickens. This thickening locally slows down the local velocity (see Eq. (4)). This is at the origin of the finger's formation (Fig. 5b–c). We found that the void tips between neighbouring fingers recede at a constant velocity $x(t) \propto t$ and govern the whole dynamics of the mean front.

For stable (straight) fronts, the driving force for dewetting was $F = -E_s L$, where L was the rim length. The simplified geometry of the unstable dewetting fronts reported in Fig. 5b–c allows us to define a mean effective driving force $-E_s \zeta$, where ζ is a typical length of the active part of the void tip. This effective force illustrates the fact that there is no more local mass conservation (as for stable fronts), but only a global mass conservation where the Si expelled from the void tips feeds the Si fingers, leading to a periodic height variation of the receding front. Using this modified model, a new expression for the velocity is derived. During the steady-state regime, the local rim at the void tip recedes with a constant height (smaller than the height of the surroundings fingers) and a constant rim width. Other parameters, such as λ and ζ, are constant for a given dewetting temperature. Following the results shown in Table 1, the measured local $x(t) \propto t$ behaviour fits our simple model.

Finally, Si fingers break down into Si nano-islands, following a scheme that could be interpreted as a Rayleigh–Plateau instability (Fig. 5a). However, as discussed in [23], standard models [45,31] underestimate the Si island formation dynamics, probably due to local Si finger tip effects.
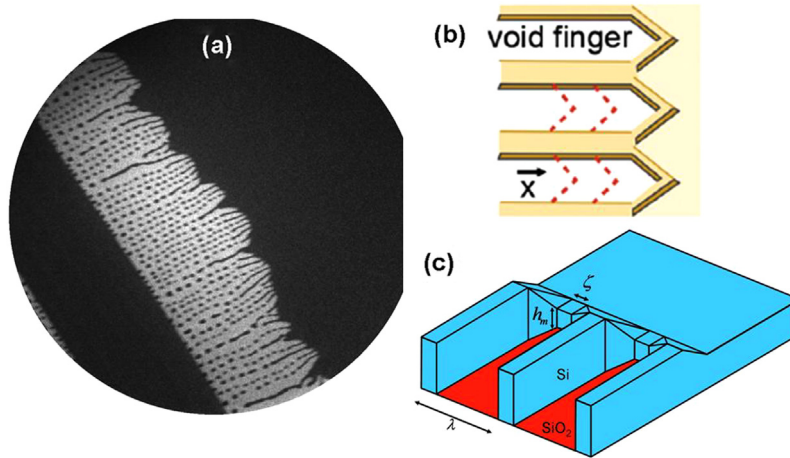
Fig. 5. Dewetting of an unstable ⟨100⟩ front digged in a Si(001)/SiO$_2$ film: (a) dark-field LEEM image (Si in dark, recovered substrate in bright, FOV: 50 μm). The mean receding front is now formed by Si elongated structures (Si fingers) separated by void fingers, as depicted in (b). In (c) is sketched a 3D view of the receding profile, where the active part of the rim (the thinner part), defining the active length ζ, can be seen.

4. Dewetting dynamics in case of heterogeneous nucleation

4.1. 2D continuous model

Far from film edges, spontaneous dewetting of 2D films is generally initiated by heterogeneous nucleation of voids at randomly distributed defects. The nucleation condition of the voids has been extensively studied in [46]. We will only here consider, from a theoretical point of view, the growth kinetics of already nucleated voids. For circular voids of radius $r(t)$, in the case of small slope approximation and in the moving referential, Eq. (1) can be written:

$$\frac{\partial h}{\partial \tau} = \frac{dr_0}{d\tau}\frac{\partial h}{\partial r} - \left[\frac{\partial^4 h}{\partial r^4} + \frac{1}{(r+r_0)^3}\left(\frac{\partial h}{\partial r} - (r+r_0)\frac{\partial^2 h}{\partial r^2} + 2(r+r_0)^2\frac{\partial^3 h}{\partial r^3}\right)\right] \tag{5}$$

with the corresponding boundaries conditions:

$$h(0) = 0$$
$$\partial h/\partial r\big|_{x=0} = \tan\theta$$
$$h(\infty) = h_0$$
$$\left[r_0^2\frac{\partial^3 h}{\partial r^3} + r_0\frac{\partial^2 h}{\partial r^2} - \frac{\partial h}{dr}\right]_{r=0} = 0 \tag{6}$$

and the velocity of the triple line:

$$\frac{dr_0}{dt} = \frac{1}{\tan\theta}\left[\frac{\partial^4 h}{\partial r^4} + \frac{1}{r_0^3}\left(\tan\theta - r_0\frac{\partial^2 h}{\partial r^2} + 2r_0^2\frac{\partial^3 h}{\partial r^3}\right)\right]_{r=0} \tag{7}$$

Eq. (5) can be numerically solved. A complete discussion can be found in Srolovitz [28], where it is shown that there are logarithmic corrections to the scaling laws $r_0(t) \sim t^\alpha$ and $h(t) \sim t^\beta$.

We report in Fig. 6 the long-time evolution of $r_0(t)$ and $h(t)$ as a function of the ratio r_0^{init}/h_0 for a given Young contact angle in a log–log diagram where r_0^{init} is the initial size of the nucleus. It can be observed that while exponent α remains more or less constant (Fig. 6), it is not the case of β (see inset in Fig. 6). The value $\alpha = 0.43$ valid for 1D model is recovered for great values of r_0^{init}/h_0, but the smaller r_0^{init}/h_0, the greater the deviation to $\alpha = 0.43$ at least at the beginning of the process. For $r_0^{init} = 0$, the asymptotic initial value of $\alpha \approx 1/4$ already reported by [28] is recovered.

However, Wong et al. [29] analytically and numerically showed that a circular hole is unstable to periodic disturbances along its perimeter, limiting seriously the capabilities of the simplified 2D model. Furthermore, because of the crystalline anisotropy, circular holes are rarely seen in experiments, so that the continuous model can only give qualitative information.

4.2. Experimental results

Experimental results for the dewetting of Si(001)/SiO$_2$ and Ge(001)/SiO$_2$ films induced by heterogeneous void nucleation can be separated into two different geometries: square void opening and dendritic void opening. These geometries will be described separately.
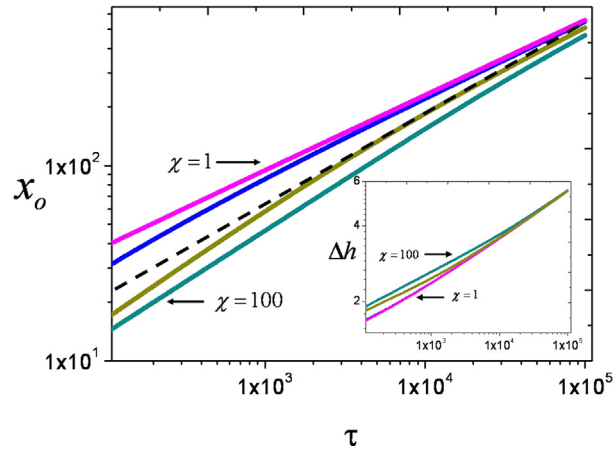
Fig. 6. Log–log plot of $r_0(\tau)$ and $\Delta h(\tau)$ calculated for different ratios of $\chi = r_0^{\text{init}}/h_0$ of 1, 10, 50, 100. The greater χ, the greater $r_0(\tau)$, but the smaller $\Delta h(\tau)$. The dotted line shows the slope $\alpha = 0.43$ (see text for details).
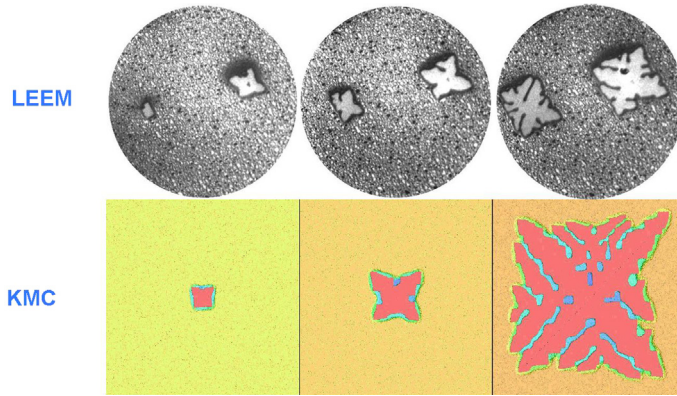

Fig. 7. Typical dark-field LEEM sequence ($\Delta t \approx 100$ s, $\Delta t \approx 700$ s, $\Delta t \approx 1400$ s, FOV = 10 μm) describing the void opening. The dark and white zones on the Si surface correspond to (1×2) and (2×1) terraces. Two voids are opening. For comparison, typical Kinetic Monte Carlo simulations from Ref. [22] reproduce well the overall morphological film evolution.

4.2.1. Void opening

Fig. 7 shows a sequence of LEEM images of the dewetting of a Si(001)/SiO$_2$ thin film. In Fig. 8a is reported a stroboscopic image, obtained from a LEEM sequence, showing the edge position during the first stages of dewetting. The dewetting process does not depend on the thickness of the film (at least in the range 10 to 22 nm). It has been largely described in the literature [5,47,9,10,22,23], so that we will simply describe a typical dewetting sequence: (1) square voids with $\langle 110 \rangle$-oriented sides nucleate heterogeneously in the Si, exposing the oxide surface (Figs. 7 and 8); (2) the voids grow spontaneously and give rise to a Si rim surrounding the void (see AFM image in Fig. 8); (3) the rim does not thicken uniformly, since the center of the void edges thicken more than the corners (see AFM image in Fig. 8, but also Fig. 2 in Ref. [48]); (4) the local thickening occurs in a layer-by-layer mode [22,23]; (5) the thickened regions recede with $r \propto t^{1/2}$, while the void corners move out at a constant velocity $r \sim t$ (see Fig. 8), so that (6) the rims undergo a shape instability forming elongated structures (called Si fingers) where mass is transferred and accumulate. Si fingers are separated by void fingers (see Figs. 7 and 8) whose tips recede at constant rim shape (constant width height and constant width rim); (7) in the long-time limit, straight Si fingers break apart, leaving Si nano-islands in their wake (see Fig. 8). Notice that in agreement with predictions depicted in Table 1, since the voids recede at constant shape, they have a constant velocity.

Finally, the complete sequence we describe is quite similar to the one reported for fronts (see Section 3.1); however, the exponents of the scaling laws are more difficult to determine accurately than for well-oriented front edges, because (i) dewetting starts at randomly distributed defects (maybe due to local stresses [49]) and (ii) local deviations due to local disturbances [29] prevent accurate long-time measurements. However, we have determined that in the long-time regime, the dewetted areas grow quadratically in time.

At first, it may seem surprising that in 2D dewetting, fingers appear on $\langle 110 \rangle$-oriented edges, while we have shown in Section 3.1 that $\langle 110 \rangle$-oriented edges are stable orientations and thus should recede without any finger formation. In fact, during the void opening, the corners of the square voids behave as precursors of $\langle 100 \rangle$-oriented void fingers limited by $\langle 110 \rangle$ microfronts, leading to a local destabilisation of the void shape, as seen in Fig. 1 and discussed in Ref. [25].
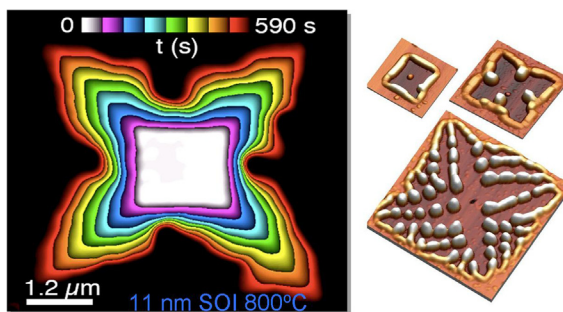
Fig. 8. Si(001)/SiO$_2$ dewetting by void opening (from Ref. [22]). (Left) stroboscopic image obtained from a sequence of LEEM images showing the shape evolution of an initial square-shaped void. The middle of the void edges recedes at lower velocity than the corners do. (Right) AFM images showing the local velocity lowering is associated with a local thickening at the origin of Si finger formation, then 3D island formation.
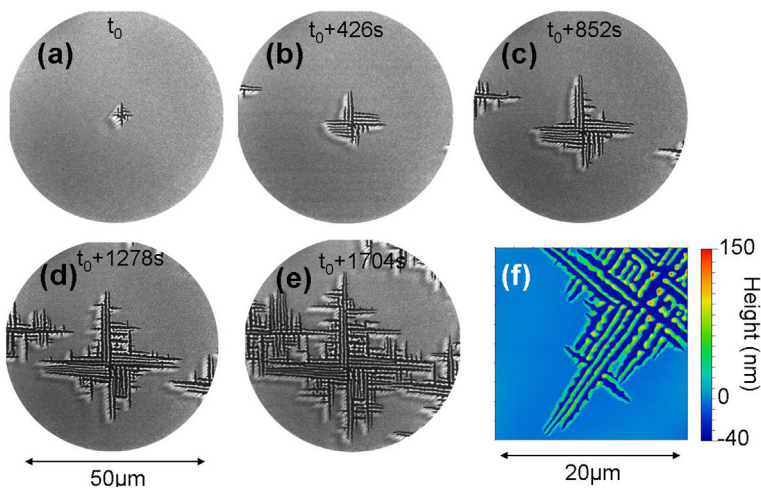

Fig. 9. Sequence of dendritic dewetting obtained for a Ge(001)/SiO$_2$ film: (a) to (e) LEEM images (bright field mode), (f) tip pattern recorded by AFM.

From a thermodynamic point of view, this set of results enable us to determine characteristic parameters of Si(001)/SiO$_2$ dewetting. The value of the driving force per front unit length is $E_s \approx 14$ eV nm^{-2} and the Si-adatom surface diffusion energy is $E_a \approx 2 \pm 0.2$ eV [23].

Fig. 7 compares a sequence of LEEM images obtained in the dark-field mode to typical Kinetic Monte Carlo (KMC) simulation results. It is clear that the KMC simulation reproduces the whole experimental shape evolution. Moreover, the dynamics of dewetting, meaning the dewetted area versus time, is also recovered (Ref. [22]).

4.2.2. Dendritic dewetting

Ge(001)/SiO$_2$ dewetting behaves differently (see Fig. 9). Indeed, if dewetting is still initiated by heterogeneous nucleation of voids, the sides of the voids now invariably turn unstable and dewetting exhibits a dendritic shape evolution (Fig. 9a). More precisely, the first stages of dewetting lead to a star-shaped dewetted area that grows linearly with time. When the branches of the star are long enough, a second lateral instability occurs and the branches of the star become ramified by the formation of secondary branches perpendicular to the first branch (Fig. 9b,c). The velocity of the principal branch's tip decreases each time a secondary perpendicular branch nucleates [50]. This in-cascade formation of branches develops a negative dendritic structure inside a square envelope (Fig. 9d) with a quadratic dependence of the dewetted area on time. Obviously, the morphology of this envelope respects the fourfold symmetry of the Ge(001) crystallographic structure. During dewetting, the matter expelled from the growing branches forms elongated structures in the ⟨110⟩ direction. The perpendicular void branches due to the secondary instability intersect these elongated structures and generate Ge nanowires or Ge nano-islands according to the branch density. The island density thus results from the dendrites branch density, that itself seems to depend on $\mu/k_BT = E_s/h_0k_BT$ (the branch density increases when μ/k_BT is lowered) [50]. Notice that a few 3D Ge-islands are also formed by periodically breaking of the longest Ge structures as in the Si(001)/SiO$_2$ system. Applying Eq. (2) to estimate the velocity of a void tip, we find for Ge at 794 °C, $D_s c_{eq} E_s \approx 4 \times 10^7$ eV s^{-1} and $E_s \approx 11$ eV nm^{-2} [50]. Notice that in Ref. [51] we carefully compare the dewetting mechanisms of Si(001)/SiO$_2$ to the dewetting mechanisms of Ge(001)/SiO$_2$.

Note that the morphological results we obtain for Ge(001)/SiO$_2$ are in qualitative agreements with models of dendritic growth that combine pure geometrical mathematical properties of a closed curve to a Landau–Ginzburg shape of
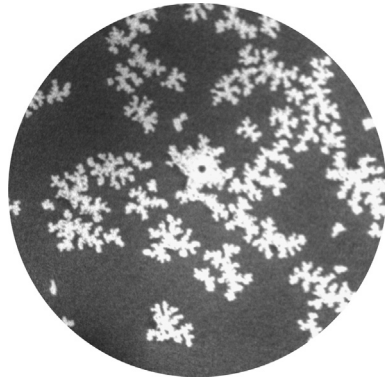
Fig. 10. Dendritic dewetting of Si(001)/SiO$_2$ ultra-thin film ($h_0 = 7 \pm 1$ nm, FOV = 25 μm).

the free-energy functional [52,53]. In particular, these models predict that each secondary tip formation lowers the velocity of the tip of the principal branch so that the side branching leads to a damped oscillatory behaviour of the tip velocity. Moreover, in this class of models, side branching only occurs when the edge anisotropy exceeds some critical value. A more realistic model developed for dendritic crystal growth [54] also shows that the lower the chemical potential change is, the greater the branch density is.

For completeness, notice that such dendritic dewetted shapes have been reported for other systems such as Ni/MgO [36] where it has been interpreted as a reminiscence of the dendritic growth observed during solidification. A similar dendrite modes has also been reported for ultra-thin Si(111)/SiO$_2$ film [55], but without clear interpretation.

4.2.3. Ultra-thin Si films

Finally, ultra-thin films seem to behave quite differently. For instance, ultra-thin Si(001)/SiO$_2$ films that we obtained by chemical etching present a fractal-like dewetting (Fig. 10). Such fractal-like behaviour has been reported for polycrystalline films such as Pt/SiO$_2$ [56], where the fractal geometry has been attributed to poor adhesion conditions of the film on its substrate or Au/SiO$_2$ [57], where the fractal-like mode has been attributed to stress-induced vacancies diffusion. Similar observations on NiAg on SiO$_2$ suggest the relevance of the mechanical stress. Indeed, while a pure Ni/SiO$_2$ ultra-thin film dewets by void growth, the addition of Ag, which is immiscible in Ni, leads to a new fractal-like dewetting [12]. Si dewetting fractals exhibit an asymptotic fractal dimension close to 1.7, also reported in Ref. [57] and compatible with Diffusion-Limited Aggregation (DLA) models. Complementary experiments on ultra-thin Si layer are needed to clarify this dewetting regime change.

5. Conclusion

Our study only concerns the dynamics of dewetting of thin films in the ideal configuration of monocrystalline films on amorphous substrates. However, as we mention in the introduction and in the main text, many other effects may influence the dewetting mechanism, e.g., grain boundaries, substrate morphology, elastic stress or thermal fluctuations (for molecular-thick films). For illustration, note that for Pt on an amorphous Si$_3$N$_4$ substrate, void formation is enhanced by a factor 9 vs. Pt on a crystalline Si$_3$N$_4$ substrate [58].

Obviously, grain boundaries may act as local defects where dewetting mechanisms are initiated. In this case, according to the grain size, the dewetted state may become labyrinthic or may present worm-like structures. However, the reciprocal is not true, since worm-like structures may have other origins than the grain boundaries.

Concerning the substrate morphology, it has been reported [17] for Ag/Si(111) that the dewetting kinetics is influenced by substrate steps. Indeed, the dewetting rate is enhanced in substrate zones of low step density because steps act as kinetics obstacles, while the initial void nucleation rate may be influenced by the local elastic deformation induced by the steps. Substrate steps may also play a role on the 3D crystal ultimately formed by dewetting. For instance, for Ag/Ru(0001) or Cu/Ru(0001) the 3D islands formed by dewetting migrate across the step edges in the downhill direction [11].

Since dewetting patterns appear to be influenced by substrate morphology, it has been proposed [18,59] to use patterned substrate to drive the dewetted patterns, i.e. to obtain 3D dewetted particles with uniform periodic spacing, size and crystallographic orientations. The already published results really open a route for tuning dewetting patterns [60,12,61].

Stress effects may also play a role. For instance, (i) local stresses associated with local defective stoichiometry or morphology may initiate the void nucleation as reported for Si(001)/SiO$_2$ by Seo et al. [49] or for Ge overgrowth on the same system [48] – maybe local stresses may also lead to a fractal-like dewetting mode, as suggested for Ni/SiO$_2$ [12], (ii) epitaxial stresses may modify the wetting factor as reported in Refs. [62,63], but also the instability mechanism [64], the kinetics [35] or the shape of the dewetted islands [65,66]. However, as discussed by Cheynis et al. [16] for most of the metastable films ($E_s > 0$), the epitaxial stress generally provides a small contribution to the total driving force of dewetting films. Despite a minor contribution to the driving force, a measurable effect on the density of 3D dewetted islands can be predicted and has

been reported [15,16]. When surface/interface energetic is unfavourable to dewetting ($E_s < 0$), it can be counterbalanced by stress effects leading to a stress-induced dewetting. It could be the case of $YBa_2Cu_3O_7/LaAlO_3$ systems [67].

Finally, in a few cases, and especially for a few monolayer-thick films, a 2D smooth film may be unstable with respect to thermal fluctuations. In this case, hole nucleation could be barrierless and the film may disrupt by spinodal decomposition. Such a behaviour has been reported for Pt/Si_3N_4 films [58] or Ag/SiO_2 [68]. However, spinodal fluctuations should lead to a statistical perfectly defined long-wave behaviour, which, generally, has not been experimentally checked in the case of solid-state dewetting.

Acknowledgements

References

[1] E. Bauer, Z. Kristallogr. 110 (1958) 372.
[2] D. Bonn, J. Eggers, J. Indekeu, J. Meunier, E. Rolley, Rev. Mod. Phys. 81 (2009) 739.
[3] E. Jiran, C.V. Thompson, J. Electron. Mater. 19 (1990) 1153.
[4] Y. Ono, M. Nagase, M. Tabe, Y. Takahashi, Jpn. J. Appl. Phys. 34 (1995) 1728.
[5] R. Nuryadi, Y. Ishikawa, M. Tabe, Appl. Surf. Sci. 159 (2000) 121.
[6] B. Legrand, V. Agache, J. Nys, V. Senez, D. Stievenard, Appl. Phys. Lett. 76 (2000) 3271.
[7] B. Legrand, V. Agache, T. Melin, J. Nys, V. Senez, D. Stievenard, J. Appl. Phys. 91 (2002) 106.
[8] R. Nuryadi, Y. Ishikawa, Y. Ono, M. Tabe, J. Vac. Sci. Technol. B 20 (2002) 167.
[9] B. Yang, P. Zhang, D. Savage, M. Lagally, G. Lu, M. Huang, F. Liu, Phys. Rev. B 72 (2005) 235413.
[10] D.T. Danielson, D. Sparacin, J. Michel, L. Kimerling, J. Appl. Phys. 100 (2006) 083507.
[11] W.L. Ling, T. Giessel, K. Thurmer, R. Hwang, N. Bartelt, K. McCarty, Surf. Sci. 570 (2004) L297.
[12] J. Petersen, S. Mayr, J. Appl. Phys. 103 (2008) 023520.
[13] A. Sundar, C. Decker, R. Hughes, S. Neretina, Mater. Lett. 76 (2012) 155.
[14] W. Tekalign, B. Spencer, J. Appl. Phys. 102 (2007) 073503.
[15] G. Capellini, G. Ciasca, M. de Seta, A. Notargiacomo, F. Evangeslisy, M. Nardone, J. Appl. Phys. 105 (2009) 093525.
[16] F. Cheynis, E. Bussman, F. Leroy, T. Passanante, P. Müller, Int. J. Nanotechnol. 9 (2012) 396.
[17] K. Thurmer, E.D. Willams, J.E. Reutt-Robey, Phys. Rev. B 68 (2003) 155423.
[18] Y. Ishikawa, M. Kumezawa, R. Nuryadi, M. Tabe, Appl. Surf. Sci. 190 (2002) 11.
[19] T. Shimura, T. Hosai, M. Umeno, J. Cryst. Growth 210 (2000) 98.
[20] K. Man, Q. Guo, M. Altman, Surf. Sci. 600 (2006) 1080.
[21] K.F. McCarty, J. Hamilton, Y. Sato, A. Saa, R. Stumpf, J. de la Figuera, K. Thurmer, F. Jones, A. Schmid, A. Talin, N. Bartelt, New J. Phys. 11 (2009) 043001.
[22] E. Bussmann, F. Cheynis, F. Leroy, P. Müller, O. Pierre-Louis, New J. Phys. 13 (2011) 043017.
[23] F. Cheynis, E. Bussman, F. Leroy, T. Passanante, P. Müller, Phys. Rev. B 84 (2011) 245439.
[24] E. Luber, B. Olsen, C. Ophus, D. Mitlin, Phys. Rev. B 82 (2010) 085407.
[25] F. Leroy, F. Cheynis, T. Passanante, P. Müller, Phys. Rev. B 85 (2012) 195414.
[26] J. Becker, G. Grün, R. Seemann, H. Mantz, K. Jacobs, K. Mecke, R. Blossey, Nat. Mater. 2 (2003) 59.
[27] W. Mullins, J. Appl. Phys. 28 (1957) 333.
[28] D.J. Srolovitz, S.A. Safran, J. Appl. Phys. 60 (1986) 255.
[29] H. Wong, P. Voorhees, M. Miksis, S. Davis, J. Appl. Phys. 81 (1997) 6091.
[30] H. Wong, P. Voorhees, M. Miksis, S. Davis, Acta Mater. 48 (2000) 1719.
[31] W. Kan, H. Wong, J. Appl. Phys. 97 (2005) 43515.
[32] E. Dornel, J. Barbé, F. de Crecy, G. Lacolle, J. Eymery, Phys. Rev. B 73 (2006) 115427.
[33] R. Bradshaw, et al., Royal Aircraft Establishment, Technical Report 66095.
[34] L. Klinger, D. Amram, E. Rabkin, Scr. Mater. 64 (2011) 962.
[35] M. Levine, A. Golovin, S. Davis, P. Voorhees, Phys. Rev. B 75 (2007) 205312.
[36] J. Ye, C.V. Thompson, Phys. Rev. B 82 (2010) 193408.
[37] D. Amram, L. Klinger, E. Rabkin, Acta Mater. 60 (2012) 3047.
[38] E. Dornel, PhD thesis, UJF, Grenoble.
[39] O. Pierre-Louis, A. Chame, Y. Saito, Phys. Rev. Lett. 103 (2009) 195501.
[40] M. Dufay, O. Pierre-Louis, Phys. Rev. Lett. 106 (2011) 105506.
[41] K. Thurmer, N.C. Bartelt, Phys. Rev. Lett. 100 (2008) 186101.
[42] N. Bartelt, R. Tromp, E. Williams, Phys. Rev. Lett. 73 (1994) 1656.
[43] G. Zinsmeister, in: R. Niedermayer, H. Mayer (Eds.), Basics Problems of Thin Film Physics, vol. 3, Vandenhoeck and Ruprech, Göttingen, 1966, p. 33.
[44] J. Venables, G. Spiller, M. Hanbücken, Rep. Prog. Phys. 47 (1984) 399.
[45] M. McCallum, P. Voorhees, M. Miksis, S. Davis, H. Wong, J. Appl. Phys. 79 (1996) 7604.
[46] D.J. Srolovitz, S.A. Safran, J. Appl. Phys. 60 (1986) 247.
[47] P. Sutter, W. Ernst, E. Sutter, Appl. Phys. Lett. 85 (2004) 3148.
[48] P. Sutter, W. Ernst, Y. Choi, E. Sutter, Appl. Phys. Lett. 88 (2006) 141924.
[49] S. Seo, C. Euaruksakul, S. Savage, M. Lagally, P. Evans, Phys. Rev. B 81 (2010) 041302(R).
[50] F. Cheynis, F. Leroy, T. Passanante, P. Müller, Appl. Phys. Lett. 102 (2013) 161603.
[51] F. Leroy, F. Cheynis, T. Passanante, P. Müller, Phys. Rev. B (2013), in press.
[52] D. Kessler, J. Koplik, H. Levine, Phys. Rev. A 30 (1984) 3161.
[53] D. Kessler, J. Koplik, H. Levine, Phys. Rev. A 30 (1984) 2820.
[54] O. Shochet, K. Kassner, E. Ben-Jacob, S. Lipson, H. Muller-Krumbhaar, Physica A 187 (1992) 37.
[55] Z. Burhanudin, R. Nuryadi, Y. Ishikawa, M. Tabe, Y. Ono, Appl. Phys. Lett. 87 (2005) 121905.

[56] P. Gadkari, P. Warren, R. Todi, R. Petrova, K. Coffey, J. Vac. Sci. Technol. 23 (2005) 1152.
[57] J.-Y. Kwon, T. Yoon, K.B. Kim, S.H. Min, J. Appl. Phys. 93 (6) (2003) 3270–3278.
[58] H. Galinski, T. Ryll, P. Elser, J. Rupp, A. Bieberle-Hutter, L. Gauckler, Phys. Rev. B 82 (2010) 235415.
[59] Y. Ishikawa, Y. Imai, H. Ikeda, M. Tabe, Appl. Phys. Lett. 83 (2003) 3162.
[60] A. Giermann, C. Thompson, Appl. Phys. Lett. 86 (2005) 121903.
[61] M. Aoussa, I. Berbezier, L. Favre, A. Ronda, M. Bolani, R. Sordan, A. Delobbe, P. Sudraud, Appl. Phys. Lett. 101 (2012) 013117.
[62] R. Kern, P. Müller, J. Cryst. Growth 146 (1995) 193.
[63] P. Müller, R. Kern, Appl. Surf. Sci. 164 (2000) 68.
[64] B. Spencer, P. Voorhees, J. Tersoff, Phys. Rev. B 64 (2001) 8397.
[65] P. Müller, R. Kern, Microsc. Microanal. Microstruct. 8 (1997) 229.
[66] P. Müller, R. Kern, Surf. Sci. 457 (2000) 229.
[67] M. Coll, J. Gaszquez, A. Pomar, T. Puig, F. Sandiumenge, X. Obrador, Phys. Rev. B 73 (2006) 075420.
[68] H. Krishna, R. Sachan, J. Strader, C. Favazza, M. Khenner, R. Kalyanaraman, Nanotechnology 21 (2010) 155601.